PUBLICATIONS OF THE ASTRONOMICAL SOCIETY OF THE PACIFIC
103: 131–149, January 1991

A SIMPLE LOW-ORDER ADAPTIVE OPTICS SYSTEM FOR NEAR-INFRARED APPLICATIONS

FRANÇOIS RODDIER, MALCOLM NORTHCOTT, AND J. ELON GRAVES

Institute for Astronomy, University of Hawaii, 2680 Woodlawn Drive, Honolulu, Hawaii 96822

Received 1990 July 9, revised 1990 September 24

ABSTRACT

It is shown that low-order wavefront compensation can significantly improve astronomical images over most of the sky. A novel approach to wavefront sensing and compensation is described. It is optimized for low-order correction and high efficiency. Computer-simulation results show it can achieve the desired performance, and preliminary laboratory tests demonstrate its feasibility.

Key words: adaptive optics–wavefront sensing–predetection wavefront compensation–high angular resolution imaging–seeing

1. Introduction

Adaptive optics (AO) is a technique to reduce image degradation produced by the turbulent atmosphere at optical wavelengths. It consists of a real-time compensation of the atmospherically induced wavefront errors. To achieve this, a reference source is needed to measure the wavefront errors by means of a wavefront sensor. The reference source can be a point source or, at the expense of some sensitivity, an extended source. In some cases the reference source can be the object under investigation itself, preferably observed in a broad-band spectral window outside the wavelength range of interest. In some other cases the reference source can be a nearby star. Compensation is achieved only in the vicinity of the reference source over an area called the isoplanatic patch. The information given by the wavefront sensor is used to drive in real time a wavefront correction device, which is usually a deformable mirror.

Although the AO technique was first proposed by Babcock 1953 for astronomical applications, until recently there have been only a few attempts to apply it to astronomy (Buffington et al. 1977; Hardy 1981; Kern et al. 1990; Rousset et al. 1990a,b). Most of the technology has been under development for more than a decade, mainly for military applications. This has two consequences, one favorable and one unfavorable. The favorable consequence is that the results obtained were impressive enough to trigger several astronomical institutions to start developing AO instruments. The unfavorable consequence is that military applications led toward expensive technological solutions not directly suitable to astronomical applications and sometimes led to misconceptions as explained below. This paper describes a low-cost, high-throughput, technical approach to AO more adapted to the needs of astronomical observations.

A common misconception is that a very large number of sensors and actuators are required to obtain images at the diffraction limit of an optical telescope. This comes from the currently used rule of thumb that to achieve diffraction-limited imaging the number of sample points must be of the order of $(D/r_0)^2$ where D is the telescope diameter and r_0 is Fried's parameter which measures the coherence length of the wavefront errors. The truth is that a significantly smaller number of sample points still produce images with a sharp core. By bringing the high spatial frequency image components above noise level it allows postdetection compensation techniques to be further used to produce perfectly diffraction-limited images. The first detailed account of the performance of low-order adaptive correction appeared in a thorough theoretical paper by Wang & Markey 1978. Later Hardy 1982 recognized and emphasized the advantage of low-order correction for astronomical application. More recently Smithson & Peri 1989 rediscovered from empirical computer simulation the high performance of "partial" adaptive correction for astronomical imaging.

By minimizing the number of sensed areas on the wavefront, one maximizes the number of photons available per sample point and the field of view over which compensation is effective (isoplanatic patch), allowing corrections to be made with fairly faint nearby reference stars. Several groups have already developed fast tip-tilt correctors or image-stabilization devices able to correct atmospherically induced image motion (Racine & McClure 1989; McClure et al. 1989; Maaswinkel et al. 1988; Brown et al. 1988; Major et al. 1990). These instruments are simply very low-order AO systems, limited to two Zernike modes (x and y tilt). They have already been successfully used to improve image quality. Although they are being used in the visible, their efficiency steeply increases at longer wavelength, as we shall demonstrate, and they are expected to become standard devices on IR telescopes. As an example the image stabilizer (HR Camera) used at the Canada-France-Hawaii Telescope (CFHT) requires a reference star brighter than 17 mag within a few arc-minutes angular distance to compensate atmospherically induced image motion. Four photomultipliers in a quadrant detector are used to sense the wavefront tilts.

By replacing the photomultipliers of the HR Camera with avalanche photodiodes one could use a reference star 2.7 mag fainter. Here we propose to extend the correction to 9 Zernike terms. We show it can be done with 13 avalanche photodiodes, thus reducing the flux per diode by a factor 4/13 or 1.3 mag. The bandwidth must be increased from 30 Hz up to 100 Hz adding a 1.3 mag loss. The total loss is 2.6 mag. *Hence, a 9 Zernike term correction should be possible with the current limiting magnitude performance of the CFHT HR Camera.* The amount of image improvement goes to a maximum at $D/r_0 = 8$ which is typically obtained at $\lambda = 1.2$ μm and occasionally in the red on Mauna Kea. As a consequence, the 3.6-m CFHT should be able to produce routinely 0\".15 stellar images in the near-infrared (1.2 μm) and occasionally 0\".1 images in the visible, using such a low-order atmospheric correction. The same order of correction applied to an 8-m telescope should routinely produce 0\".15 images from 1.6 to 3.5 μm and occasionally 0\".1 images at 1.2 μm. However, more photons being available with a larger telescope, it is possible to proceed with higher-order corrections and again obtain routinely 0\".15 stellar images at 1.2 μm and occasionally 0\".1 images in the visible, with a 17-mag reference star.

Because we limit ourselves to low-order corrections, the field of view over which the correction is effective (isoplanatic patch) remains reasonably large, typically one arc minute, and a reference star of appropriate magnitude will often be present within the limits of this field. Because the order of correction required to get sharp images is commonly overestimated, the size of the isoplanatic patch is accordingly underestimated. Moreover, currently proposed systems have a poor throughput and a corresponding low probability of finding appropriate reference stars. This led to the idea of producing artificial light spots in the atmosphere by laser illumination and using these spots as a reference. However, owing to foreshortening effects, the artificial star technique is difficult to implement on large telescopes (4 meter and above) whereas on smaller telescopes it directly competes with the Hubble Space Telescope. We believe that the approach we propose here is both more realistic and more cost-effective.

The theoretical performance of low-order adaptive corrections is reviewed in Section 2, and the goal we propose to achieve is specified. A few examples of astronomical applications are described in Section 3. How this goal can be optimally achieved is discussed in Section 4, where a new type of AO system uniquely designed for this purpose is described. Results already obtained are presented in Section 5. They include both computer simulations and laboratory results.

2. Expected Performance

2.1 *Strehl Resolution*

The performance of an AO system is best defined in terms of the maximum intensity obtained in a point-source image. The ratio of this intensity to the maximum intensity in the diffraction-limited image (Airy pattern) is called the Strehl ratio. Assuming the total flux is unity, the maximum intensity in a point-source image is currently referred to as the Strehl resolution (see, for instance, Babcock 1990). In the case of atmospheric compensation it is convenient to normalize the Strehl resolution R by dividing it by the maximum Strehl resolution R_{max} one can achieve without compensation. R_{max} is the Strehl resolution for long exposures made with an infinitely large telescope through the uncompensated atmosphere. The Strehl resolution R achieved by an AO system depends on both the telescope diameter D and the Fried seeing parameter r_0. However, the normalized resolution R/R_{max} depends solely on the ratio D/r_0 and is an excellent measure of the performance of the system.

In his early publication, Fried 1966 gives the first theoretical estimate of the normalized Strehl resolution R/R_{max} for tip-tilt corrections as a function of D/r_0. A log-log plot is given in Figure 1 of his paper (the near-field case is the case which best applies to astronomical observations). Wang & Markey 1978 generalized Fried's results to higher-order Zernike terms. For convenience Table 1 shows the Zernike aberration terms discussed in this paper. They are also displayed in Figure 9. Using a Monte Carlo technique, Nicolas Roddier 1990 has recently computed R/R_{max} ratios as a function of D/r_0 up to a 9 Zernike term correction, fully confirming Wang and Markey's results. A log-log plot of some of the results is reproduced here in Figure 1.

A wavelength scale is given on top of Figure 1 to show the wavelength dependence of r_0. It has been set to represent D/r_0 at the CFHT under *average* seeing conditions (0\".71 images or $r_0 = 14.4$ cm at 0.5 μm). By translating this scale horizontally (for instance on a transparent overlay) one can set it to any telescope diameter or seeing condition. It shows that, under average seeing conditions at CFHT, a 9-Zernike correction has its maximum efficiency at 1.2 μm with a gain in central intensity of more than 3 stellar magnitudes over the uncompensated case. Tip-tilt correction alone has its maximum efficiency at 2.2 μm with a gain approaching 2 magnitudes. It should be stressed that these performances are highly seeing dependent. To illustrate this point, we have also plotted in Figure 1 a distribution of D/r_0 at 0.5 μm observed at the

TABLE 1
Low Order Zernike Aberrations

Radial degree (n)	Azimuthal frequency (m) 0	1	2	3
0	Z_1 Piston			
1		Z_2, Z_3 Tip-tilt		
2	Z_4 Defocus		Z_5, Z_6 Astigmatism	
3		Z_7, Z_8 Coma		Z_9, Z_{10} Triangular coma
4	Z_{11} Spherical aber.		Z_{12}, Z_{13}	

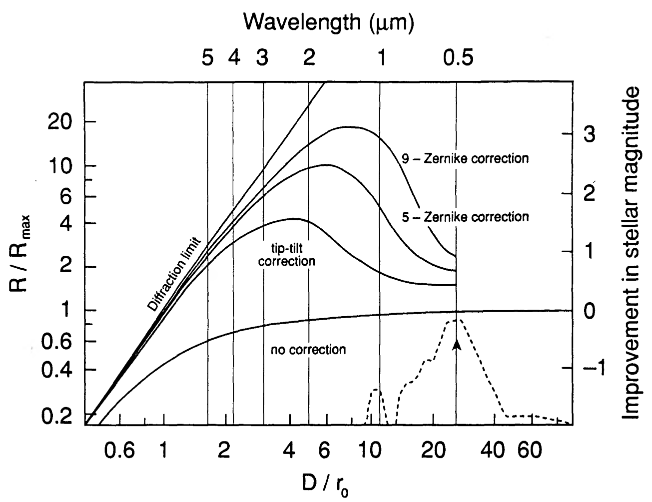

FIG. 1–Theoretical curves showing the normalized Strehl resolution R/R_{max} as a function of D/r_0, the ratio of the telescope diameter over Fried's seeing parameter. R/R_{max} is the stellar image central intensity normalized to unity for an infinitely large uncompensated telescope. Curves are for several degrees of compensation. The vertical scale on the right side gives the improvement over the uncompensated case in stellar magnitude. The upper scale indicates the wavelength dependence of D/r_0. It is set for D = 3.6 m (CFHT) and a seeing value of r_0 = 14.4 cm at 0.5 μm and it can be moved horizontally according to seeing conditions. For example, if r_0 = 36 cm at 0.5 μm (which occasionally occurs) then the wavelength scale is shifted to the left with 0.5 μm set to D/r_0 = 10. The dotted curve in the lower right corner shows a statistical distribution of D/r_0 observed at 0.5 μm at the CFHT and it can be moved horizontally to show the statistical distribution of D/r_0 at a different wavelength as pointed by the arrow.

CFHT during a campaign of seeing measurements in June 1989 (Roddier, F. et al. 1990a). Stellar images smaller than 0.″5 ($D/r_0 \leq 17.5$) are observed about 20% of the time at CFHT in which case a 9-Zernike correction has its maximum efficiency in the red.

2.2 *Image Widths and Profiles*

Astronomers are used to measuring image quality in terms of stellar image full width at half-maximum (FWHM). This is a reasonable criterion as long as the image photometric profile does not change. However, partial wavefront correction tends to produce sharp images with a variable amount of light scattered in the wings of the stellar profile, which the FWHM criterion does not take properly into account. A better measure of the image width that takes the wings into account is the Strehl width which is defined as the width of a uniformly illuminated disk with the same total flux and the same intensity (i.e., same Strehl resolution). The Strehl width of an Airy pattern is 1.27 λ/r_0. Figure 2 shows the expected Strehl width at the CFHT as a function of wavelength for a 9-Zernike correction and for tip-tilt correction only. Figure 2a is for typical seeing conditions and Figure 2b is for good seeing conditions. They show that under typical seeing conditions a 9-Zernike correction will produce 0.″15 Strehl width images at 1.2 μm, whereas under good seeing conditions it will produce 0.″1 Strehl width images in the red. Note that nearly perfect diffraction-limited resolution is achieved at 1.2 μm for average seeing and at 0.7 μm for good seeing conditions with only a 9-Zernike correction. *This is the basis for proposing to develop low-order AO systems for astronomical applications.*

We have computed stellar image profiles with various degrees of correction at maximum efficiency. They are presented in Figures 3 and 4. In all cases the Strehl ratio approaches 0.3. The horizontal scale is in arc seconds for the CFHT operating at 1.2 μm. Figure 3a shows the effect of tip-tilt correction only (image stabilization) when D/r_0 = 4 or r_0 = 90 cm. This corresponds to r_0 = 31.5 cm at 0.5 μm, a seeing value which has been effectively observed at the CFHT during the June 1989 campaign (Roddier, F. et al. 1990a). Figure 3b shows the effect of a 5-Zernike correction (1st- and 2nd-degree Zernike polynomials) when D/r_0 = 6 or r_0 = 60 cm, which corresponds to r_0 = 21 cm at 0.5 μm. Figure 4a shows the effect of a 9-Zernike

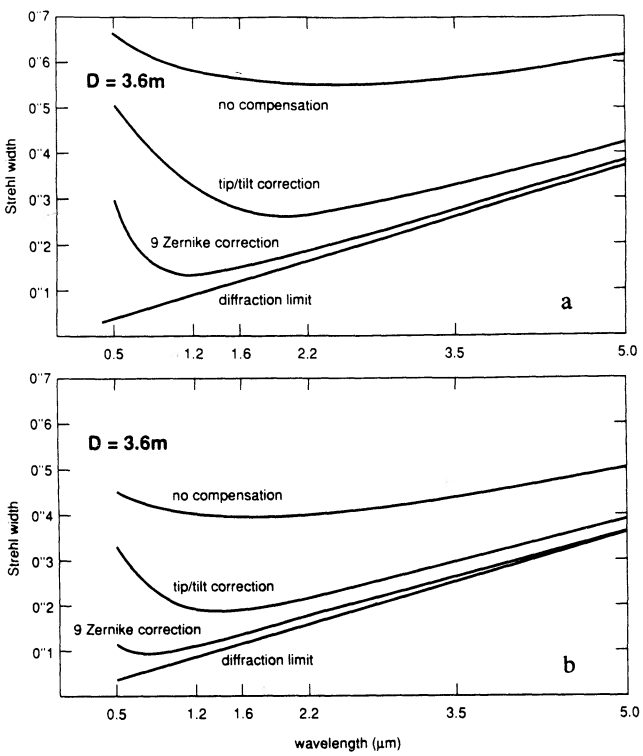

FIG. 2–Calculated Strehl width as a function of wavelength for a 3.6-m telescope with various degrees of compensation. The uncompensated Strehl width at 0.5 μm is assumed to be 0.66 arc second (a) or 0.45 arc second (b).

correction (up to 3rd-degree Zernike polynomials) when $D/r_0 = 8$ or $r_0 = 45$ cm, which corresponds to $r_0 = 15.7$ cm or 0."65 uncompensated images (FWHM) at 0.5 μm, a value often reached at Mauna Kea. At 1.2 μm the compensated image FWHM is 0."075 and the gain in central intensity over the uncompensated case is 3.3 magnitudes. For comparison Figure 4b shows the actual performance of the proposed AO system as obtained from computer simulations (see Section 5.1).

2.3 *Performance Limitations*

The above-described performance applies as long as the reference wavefront exactly matches the wavefront to be compensated. Increasing time delays between wavefront measurements and wavefront corrections or increasing distance between the reference star and the object produce increasing differences between the two wavefronts which degrade the system performance. The quality of the correction is set by the degree of correlation between the two wavefronts. Let ϕ be the wavefront phase error associated with the object, which is to be corrected, and let ϕ_e be the wavefront phase error estimated from the reference star. After correction the total mean square error is

$$< |\phi - \phi_e|^2 > = < |\phi|^2 > + < |\phi_e|^2 > - 2 < |\phi\phi_e|^2 > \ . \qquad (1)$$

Since the wavefront from the object and the wavefront from the reference have the same statistical fluctuations,

$$< |\phi|^2 > = < |\phi_e|^2 > \ . \qquad (2)$$

Hence, equation (1) can be written

$$< |\phi - \phi_e|^2 > = 2\,(1 - \Gamma) < |\phi|^2 > \ , \qquad (3)$$

where

$$\Gamma = \frac{< |\phi\phi_e|^2 >}{< |\phi|^2 >} \qquad (4)$$

is the degree of correlation between the two wavefront errors. In order to get some image improvement, the mean square wavefront phase error must be smaller after correction:

$$< |\phi - \phi_e|^2 > \leq < |\phi|^2 > \ . \qquad (5)$$

Putting equation (3) into equation (5) gives $\Gamma \geq 0.5$. In other words, the wavefront errors must be correlated by more than 50%. We shall discuss the effect of a time delay first and then the effect of the angular distance between the object and the reference source (isoplanicity).

2.3.1 *Time Delay Errors*

The speed at which the correction has to be made is an important parameter in adaptive wavefront compensation. It will ultimately set the limiting magnitude of the reference source which can be used. To get information on the speed at which wavefront errors must be corrected, a special seeing monitor was built and operated during several nights at Mauna Kea in June 1989 (Roddier, F., Graves & Limburg 1990b). The monitor recorded the time evolution of the wavefront local curvature on a 20-cm pupil. Because adjacent wavefront curvatures are nearly uncorrelated, their evolution time is a good indicator of the speed required for adaptive wavefront compensation. Moreover, the sensor we propose below being based on wavefront curvature measurements, the results obtained in June 1989 are directly relevant to this proposal.

Figure 5 shows characteristic examples of autocorrelation function of the time evolution of the wavefront curvature recorded in June 1989 on a 20-cm pupil. Note the steep decrease of the autocorrelation near the origin. It drops to 50% of the value at the origin in typically 3 milliseconds. Atmospheric turbulent layers were simultaneously monitored using the "scidar" technique (Roddier, F. et al. 1990a) and we were able to show that this fast decay is essentially due to turbulence in the free atmosphere which is associated with high-speed winds and contributes to nearly 40% of the image degradation. Being an excellent site, Mauna Kea has a remarkably low turbulence boundary layer, which implies that a larger-than-usual fraction of image degradation comes from high-altitude layers. The slower decay observed at longer

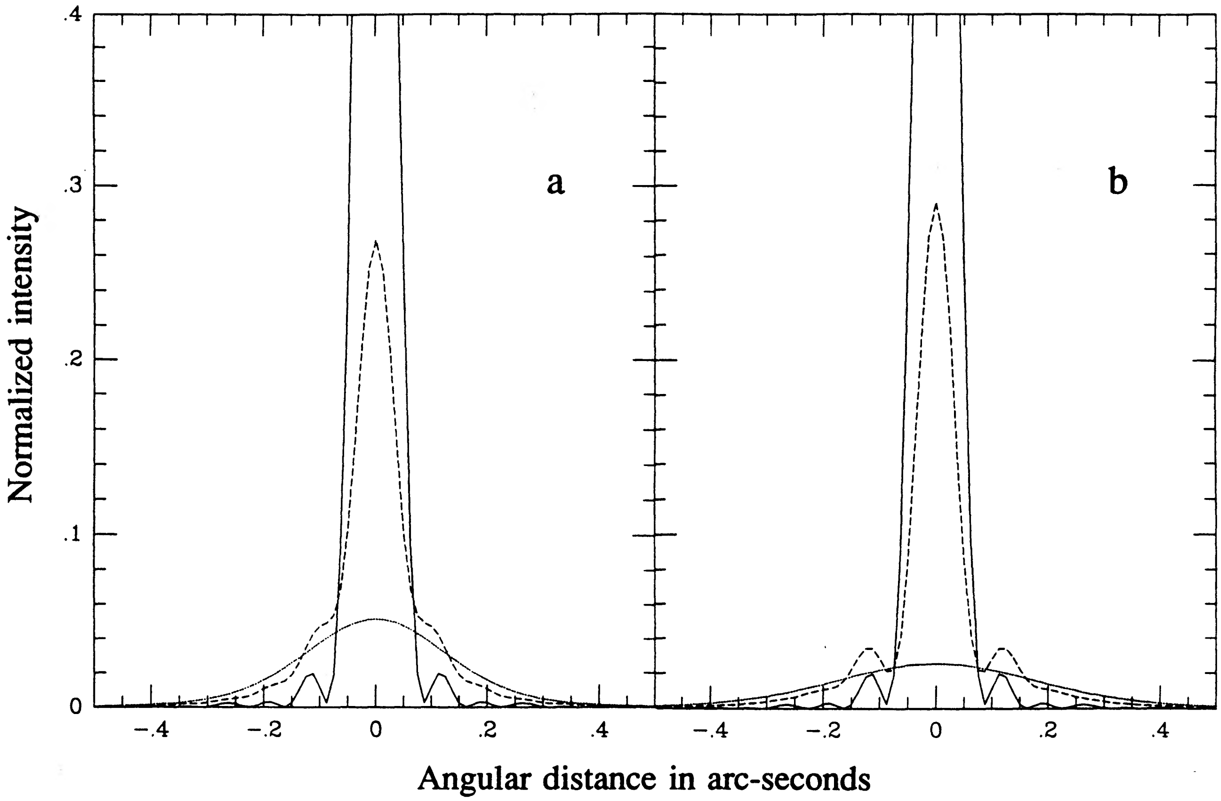

FIG. 3–Theoretical stellar image profiles for an uncompensated (dotted line), compensated (dashed line), and diffraction-limited (full line) image: (a) is for a 1st degree (2-Zernike) tip-tilt only correction when $D/r_0 = 4$; (b) is for a 2nd degree (5-Zernike) correction, which includes defocus and astigmatism, when $D/r_0 = 6$. The vertical scale is normalized to unity at the maximum of the diffraction-limited image. The horizontal scale is in arc seconds for a 3.6-m telescope at $\lambda = 1.2$ μm. The FWHM seeing angles at 0.5 μm are, respectively, 0.32 arc sec (a) and 0.48 arc sec (b) values occasionally observed at the CFHT.

time lags is produced by local turbulence which propagates more slowly. Figure 6 shows a histogram of the 50% correlation time obtained from curves such as Figure 5 over a few nights of observations. It indicates that a 2-millisecond response time is required to make corrections over a 20-cm diameter area. Since we plan to make corrections over 1-m diameter areas this time is increased to 10 milliseconds. This is faster than the European "COME-ON" experiment (Rousset et al. 1990a,b). It seems that the speed required for adaptive wavefront compensation has generally been underestimated.

Knowing the space and time scale over which the wavefront has to be compensated, one can estimate the magnitude of the reference star required. We plan to use an array of discrete avalanche photodiodes which will collect and count photons from 500 to 900 nm. To achieve a 9-Zernike correction on a telescope such as the CFHT, each diode will sense the wavefront over a 1 m^2 area. Computer simulations show that the sensor will still operate reasonably well with 50 counts per response time (Roddier & Roddier 1989). Assuming a 10-millisecond response time, this gives 5×10^3 counts per second. The light budget detailed in Section 4.4 shows that this count rate can be obtained with a 16-mag star. Moreover, Figure 6 shows that 24% of the time the 50% correlation decay time is at least 25 msec for a 1-m aperture in which case one can use a star one magnitude fainter. In the following we consider $m = 17$ as the limiting magnitude for a 9-Zernike correction with the proposed AO system, keeping in mind it can be reached 24% of the time. Using tip-tilt correction only, one can still get a substantial image improvement (as shown above) using 2.25 m^2 areas and a time constant about three times longer which brings the limiting magnitude up to more than 19. This is entirely consistent with the present performance of the CFHT HR Camera (image stabilizer) (Racine & McClure 1989; McClure et al. 1989), assuming that the current photomultipliers are replaced with avalanche photodiodes.

2.3.2 *Isoplanicity*

Another important parameter in adaptive wavefront compensation is the field of view over which image improvement can be achieved. This field called the isoplanatic patch sets the fraction of the sky over which image improvement can be achieved. It depends on the degree of correction required and is determined by the angular decorrelation of Zernike aberration terms. Figure 7 shows the correlation between wavefront tilts as a function of the angular distance between the two sources for a

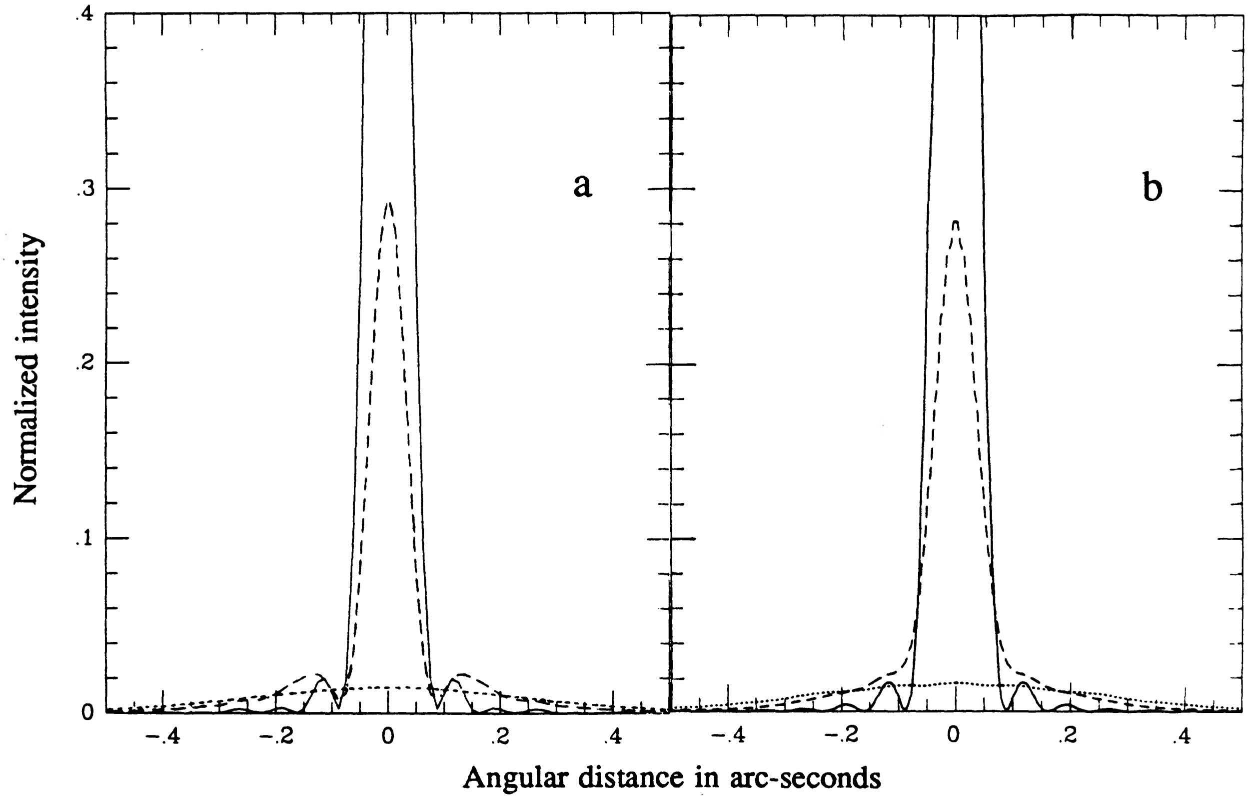

FIG. 4–Theoretical (a) and computer-simulated (b) stellar image profiles for an uncompensated (dotted line), compensated (dashed line), and diffraction-limited (full line) image, assuming $D/r_0 = 8$. For the compensated image, the theoretical profile is for a 9-Zernike correction. The computer simulated profile was obtained by taking the azimuthal average of the compensated image shown in Figure 18 ($D/r_0 = 8$ case). The vertical scale is normalized to unity at the maximum of the diffraction-limited image. The horizontal scale is in arc second for a 3.6-m telescope at $\lambda = 1.2\ \mu$m with a seeing angle of 0″.65 at 0.5 μm.

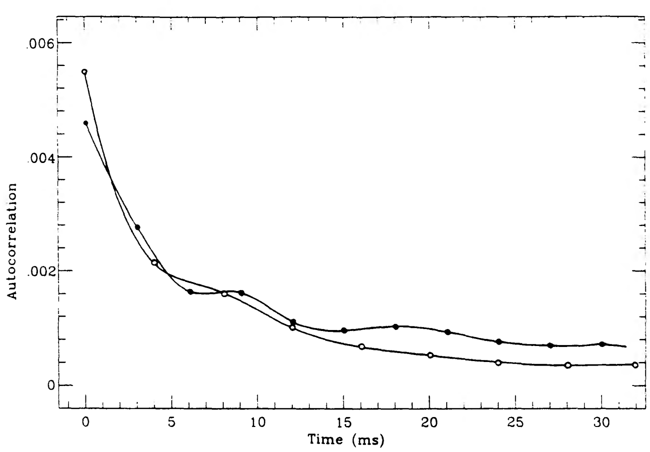

FIG. 5–Two examples (open and full circles) of autocorrelation functions of the time evolution of the wavefront curvature over a 20-cm diameter pupil. Data were taken on Mauna Kea in June 1989. The vertical scale is arbitrary.

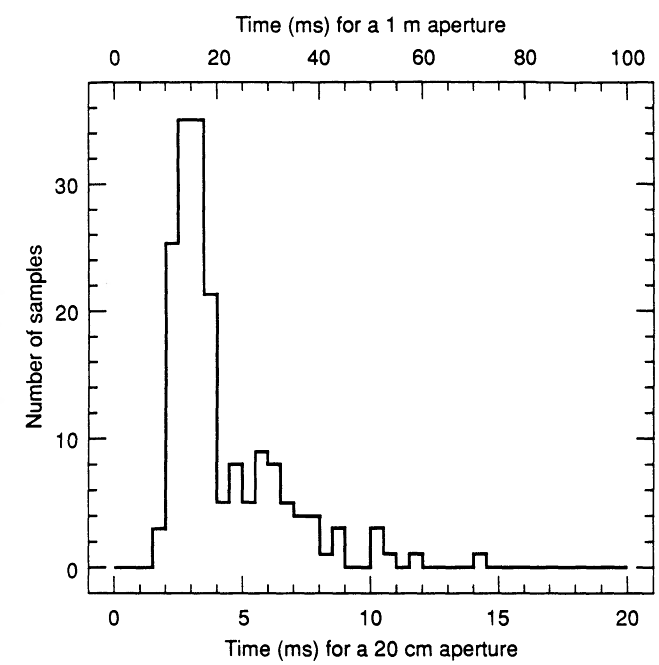

FIG. 6–Histogram of the 50% correlation decay time measured on autocorrelation curves such as shown in Figure 5. The histogram was obtained over four nights of observations on Mauna Kea. The bottom scale is the actual decay time observed through the 20-cm aperture used in this experiment. The upper scale is the 5-times longer decay time one would observe over a 1-m aperture.

3.6-m telescope. The curves are based on theoretical calculations by Valley & Wandzura 1979. Note that the longitudinal correlation (in the direction of the tilt) drops faster than the lateral correlation (in a direction perpendicular to the tilt). This is expected to produce images slightly elongated in the direction of the reference star, a small effect recently detected with the CFHT HR Cam-

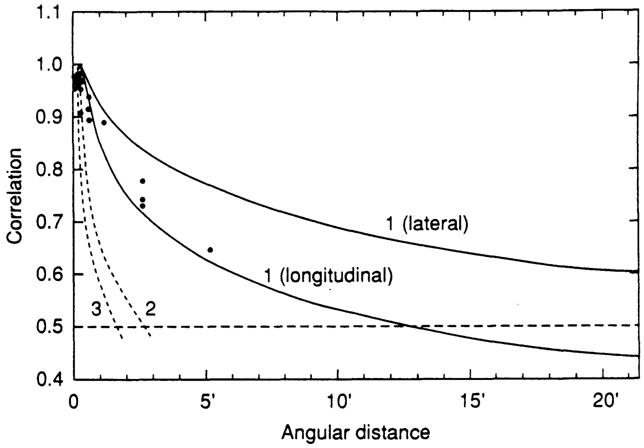

FIG. 7–Correlation between the Zernike components of wavefronts as a function of the angular distance between the sources. (1) Longitudinal and lateral correlation for tilts. (2) Average correlation for 2nd degree Zernike terms. (3) Average correlation for 3rd degree Zernike terms. Full lines are from Valley & Wandzura 1979. Dashed lines are from Chassat 1989. Dots are experimental points published by Christian & Racine 1985 for the longitudinal tilt correlation. The horizontal scale is for a 3.6-m telescope.

era (McClure, private communication). The dots are experimental points for the longitudinal correlation. They were obtained at the CFHT by Christian & Racine 1985. The longitudinal correlation probably drops down to 50% at 13 arc minutes or more. It shows that the field over which some image improvement can be expected at CFHT has a typical diameter of at least 26 arc minutes. This improvement can be obtained with a reference star up to 19 mag which permits one to easily cover the whole sky.

One may then ask over which fraction of the sky can we take advantage of a 5- or 9-Zernike term correction (up to radial degree 2 and 3)? Chassat 1989 has recently calculated the angular correlation of higher Zernike modes. Using an average turbulence model from Hufnagel 1974, he found that for a 1-m-radius aperture a 5-Zernike correction (up to radial degree 2) can be applied up to a distance of 44×10^{-5} radian. Since the angle is proportional to the telescope diameter, this corresponds to a 5.4-arc-minute-diameter field at CFHT. Similarly, a 9-Zernike correction (up to radial degree 3) can be applied up to a distance of 27×10^{-5} radian or cover a 3.3-arc-minute-diameter field at CFHT. It means that over such a field of view a 9-Zernike correction will produce the optimum overall image improvement. Since there is statistically at least one star with magnitude equal to or brighter than 17 in such a field, this order of correction is appropriate over the whole sky without ever having to switch back to a lower-order correction.

Clearly the amount of image improvement steeply decreases as the distance from the reference star increases. Experience with the CFHT HR Camera shows that a noticeable image improvement can be seen up to the edge of the 1.7 arc minute CCD field of view when the reference star is located at the opposite edge and the telescope is stopped down to 1.2 m. For a 3.6-m telescope, this corresponds to a 5-arc-minute distance or a field-of-view diameter of 10 arc minutes. At the edge of such a field the average degree of correlation of wavefront tilts is 70%. Chassat's curves, indicated with a broken line in Figure 7, show the distance over which the same amount of average correlation is expected for higher-order corrections. For a 5-Zernike correction (up to radial degree 2), it corresponds to a 1.5-arc-minute diameter field of view and for a 9-Zernike correction (up to radial degree 3) it corresponds to a 50-arc-second-diameter field of view. This is the field over which a correction starts to be really effective compared to lower-order corrections. Table 2 summarizes these results indicating the estimated limiting magnitude, field of view, and percentage of sky coverage for various degrees of correction.

The limited size of the isoplanatic patch is eventually a severe limitation to AO. However, as shown in Table 2, it is not as severe as it is generally thought. This is because we have limited ourselves to low-order corrections. Moreover, the size of the isoplanatic patch *can be further increased* up to typically a factor two depending on seeing conditions by reimaging dominating turbulent layers onto the deformable mirror as described in Appendix A.2. Table 2 does not take this important possibility of improvement into account.

2.4 *Sky Coverage*

As the degree of correction increases, both the field of view over which the correction is effective and the limiting magnitude for the reference star decrease. Figure 8 shows the limiting magnitude and the field of view (at 70% correlation) for various radial degrees of correction at the CFHT (hatched boxes). The size of the boxes allows for variations in seeing conditions. Full lines show the limit at which one can find on average one reference star per field of view either at the Galactic pole or at the Galactic

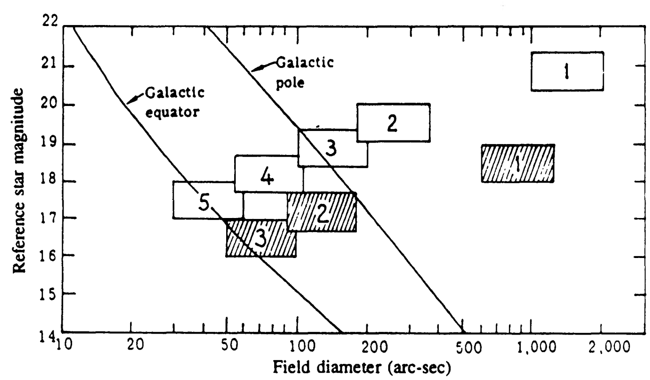

FIG. 8–Field of view and reference-star limiting magnitude for various radial degrees of correction as indicated in the boxes. The size of the boxes allows for variations in seeing conditions. Hatched boxes: CFHT. Open boxes: 8-m class telescope. The curves indicate the limits at which one will find one reference star per field (on average).

TABLE 2
Field Over Which Image Correction Applies. This Field Can Be Further Increased by Instrumental Tuning (see Appendix Part B)

		1	2	3
Radial degree of correction		1	2	3
Number of Zernike modes corrected		2	5	9
Limiting magnitude for reference star		19	18	17
Av. correlation over 50% {	field diam.	1°	5.4'	3.3'
	% of sky	100%	100%	100%
Av. correlation over 70% {	field diam.	10'	1.5'	50"
	% of sky	100%	84%	37%

equator. Clearly, going to a radial degree higher than three would apply only to a few objects in the sky and may not be worth the investment. The percentage of sky coverage indicated in Table 2 was obtained by integrating the star distribution over the whole sky. Note that these results are independent of the wavelength considered. Figure 8 also shows the values for an 8-m class telescope. In this case one will probably wish to correct up to 5th-degree Zernike polynomials (21 terms) which can be done with 37 sensors and actuators using the same technique as we propose.

2.5 *Detection Threshold*

So far we have only discussed the limiting magnitude for the reference source, not for the object sources. By sharpening the images, adaptive optics will help detect small objects against the sky background and improve the limiting stellar magnitude of telescopes. Following the approach of Tokunaga 1989, we have estimated the limiting magnitude of CFHT with detector arrays operating at various wavelengths, with and without AO compensation. The sky background was taken from Tokunaga 1989 in the IR and from Lena 1988 at shorter wavelengths. In all cases we assume a resolving power $\lambda/\Delta\lambda = 5$. The Strehl width was taken to be 0".45 at 0.5 μm ($r_0 = 29$ cm), and in each case the pixel width was taken equal to the Strehl width indicated in Figure 2b. The results are shown in Table 3. The instrumental efficiency includes both the optics and the detector quantum efficiency. Whenever AO compensation is used, it has been reduced to 80% of its original value to allow for the efficiency of additional optics. The limiting magnitude (1 σ) is for a total integration time of 1800 seconds.

3. A Few Examples of Astronomical Applications

As discussed in Section 2, low-order AO compensation can improve the angular resolution of a telescope such as the CFHT by a factor 5 under average seeing conditions and can improve by a factor 3 the best images obtained with the HR Camera. Being able to use a mag 17 star as a reference allows the compensation to be achieved over a large fraction of the sky. It is impossible to do justice in this section to the scientific importance of such a performance enhancement which encompasses almost all of astronomy. We only give here a few examples which have been suggested to us by our colleagues already enthusiastic about the potential of adaptive optics. We acknowledge their assistance in writing this section.

By the time of this writing the Hubble Space Telescope (HST) has been put in orbit and is not achieving the expected resolution performance. It is hoped that the problem will be eventually solved, in which case many objects considered below will certainly be also observed with HST. However, observing time will be very limited and the collecting power will be that of a 2.4-m telescope. While providing a comparable level of angular resolution, AO on ground-based telescopes will permit longer-term observations, will provide more collecting power (which

TABLE 3
The Effect of Adaptive Optics on Sky Background and Telescope Limiting Magnitude

Wavelength (μm)	0.70	0.90	1.25	1.65	2.20
Detector material	Si	Ge	HgCdTe	HgCdTe	HgCdTe
Read-out noise (e-)	10	50	50	50	50
Without adaptive optics					
Instrum. efficiency	0.45	0.35	0.35	0.35	0.35
Pixel width (arc-sec.)	0.43	0.41	0.40	0.40	0.40
Background (e-/sec.)	100	660	1500	5750	3200
Limiting magnitude	28	26.4	25.7	24.4	24.2
With adaptive optics					
Instrum. efficiency	0.35	0.25	0.25	0.25	0.25
Pixel width (arc-sec.)	0.10	0.10	0.11	0.14	0.18
Background (e-/sec.)	4	27	80	500	460
Limiting magnitude	29.4	27.7	26.9	25.4	24.9

is essential for narrow-band imaging and spectroscopic applications), and will utilize state-of-the-art detector arrays. Furthermore, it will permit the HST to concentrate fully on observations which can be made only from space, or for which telluric absorption or emission is a major concern.

3.1 *Young Stellar Objects*

At the distance of the nearest star-forming region (in Taurus) 0.1 to 0.2 arc sec represents 15 to 30 AU. With such a resolution one can expect a breakthrough in the study of stellar and planetary formation. AO will allow us to explore both the morphology and the kinematics of optical jets and circumstellar disks on a sample of objects large enough to cover different ages with a good representation. It will permit a systematic search for companions of T Tauri stars and allow us to determine the binary frequency as a function of separation, indicating under which condition a companion star forms rather than planets. At orbital distances of 15 to 30 AU, orbital motion could be followed in a reasonable amount of time and give us accurate mass estimates of the young low-mass stars which are needed to calibrate tracks in the H-R diagram and test pre-main-sequence star theory. In most cases the main star will provide enough photons to sense the wavefront. However, because of the strong extinction observed in star-formation regions, the red sensitivity of the photodiodes will be essential. In some cases one may have to rely on a close foreground star.

3.2 *Galactic Center*

The Galactic center is an excellent candidate for high-resolution imaging. Here extinction is so large (25 mag in the visible) that one has to rely on foreground stars to sense the wavefront. Kern et al. 1988 have shown that there are enough such stars of mag 15 or brighter to cover most of this region. This will enable us to produce high-resolution infrared images of the Galactic center and to study its mass distribution. It will perhaps allow us to answer the important question of whether or not there is a massive nonstellar object at the center of our Galaxy.

3.3 *Globular Clusters*

Advances in the study of the dense, crowded cores of globular clusters are entirely dependent on the achievement of the highest spatial resolution: identification and monitoring of X-ray sources, investigations of the stellar constituent of the cores, tests of dynamical models of core evolution, radial dependence of the stellar luminosity functions, and studies of hard binaries and coalesced stars. All of these questions bear on our understanding of the first objects to be formed out of the pristine protogalactic material. In most cases a nearby star or the center of the cluster itself will provide appropriate reference.

At an angular resolution of about 0.1 arc sec, globular clusters with a 10-pc radius will be distinctly nonstellar out to distances as large as 40 Mpc. Cluster systems will be identified and studied around many galaxies of all types, free of the uncertainties associated with statistical subtraction of field contamination. This will result in much-improved characterization of the cluster systems, securing their use as indicators of extragalactic distances and of early galactic evolution. Delineation of the maximum size that globulars can achieve will impact the theories of their formation. The outer regions of globulars in all Local Group galaxies will be easily resolved into stars. Precision color-magnitude diagrams reaching below the subgiant branch will allow us to determine their ages. Cluster variables can be studied and compared to those in the Milky Way and the Magellanic Clouds.

3.4 *Study of Galaxies*

One of the most exciting applications of adaptive optics will be in the imaging and spectroscopy of galaxies. Active galactic nuclei and cores of normal galaxies are especially amenable to study with this technique. It will allow us to measure velocity dispersion very close to the center of galaxies such as M 31 and M 32 and to check the black-hole hypothesis. HST time has been granted to look for black holes using the Faint Object Spectrograph; but even with a 0.25 arc-sec-square aperture, exposure times on the brightest galaxies will be about 2 hours per position. Almost no galaxy has a surface brightness high enough to allow the use of the 0.1 arc-sec-square aperture. In 1991 the new Subarcsecond Imaging Spectrograph will become available on the CFHT. It will have optics capable of FWHM values of about 0.15 arc sec. Therefore, the spatial resolution expected to be achieved in practical exposures with HST is no longer an intimidating goal.

The scale length of a galaxy profile at $z \approx 1$ should be larger than 0.2 arc sec. On a 3.6-m telescope, AO will provide a resolution of 0.5 kpc at $z = 1.25$ and should be able to resolve spiral arms anywhere in the universe. High-angular-resolution observations will allow us to investigate the evolution of galaxies over a look-back time greater than 80% of the age of the universe. Large aperture and high resolution will make it possible to observe the relation between the apparent size of galaxies and their redshift, a crucial test of the geometry of the universe. The deepest 2.2-μm images already show all the galaxies seen in the visible. With adaptive optics it will become possible to see fainter sources with a higher resolution. For instance, one should be able to detect photogalaxies with K magnitude 22 to 24 (see Table 3). The study of multiple, gravitationally lensed images of distant quasars seen through galactic gravitational potentials will also greatly benefit from very high angular resolution, as recent discoveries made possible by the 0.6 arc sec resolution of the CFHT have already demonstrated.

4. An Optimized System

4.1 *Optimizing System Performance*

Wavefront perturbations can be expanded in a series of orthogonal functions such as Zernike modes, or any orthogonal linear combination of Zernike modes. Among all these possible sets of orthogonal functions, there is only one set which consists of statistically independent perturbations. The functions of that set are called the Karhunen-Loeve functions. Figure 9 is a display of the lower-order Karhunen-Loeve modes together with the same-order Zernike modes for comparison. Any real AO system has a finite number of correcting elements and, therefore, corrects only a finite number of modes. Mathematically, one can show that the most effective AO system is the one which will best correct the low-order Karhunen-Loeve modes. The system we propose to build has been optimized with this goal in mind.

The cost of an AO system grows in proportion to the number of actuators and sensors (or wavefront measurements) so that every effort should be made to minimize these numbers. Moreover, minimizing the number of sensors will also minimize sensor noise and maximize speed which will improve system performance. However, undersampling produces errors due to aliasing. To minimize undersampling errors one must optimize the actuator and sensor geometry. The ratio of the number of compensated modes over the number of wavefront corrections can be taken as a measure of the degree of system optimization. Theoretically, this number could be unity. For currently planned systems it is below 0.5. For the system we propose here it reaches 0.7. In addition, the response of a wavefront sensor is, in general, nonlinear. In order to operate in its linear range the sensitivity of the wavefront sensor must be adjusted to seeing conditions. In general this cannot be done, even manually. The sensitivity of the novel wavefront sensor described below has the unique capability to automatically adjust itself to changing seeing conditions, constantly keeping the sensor in its optimum linear range.

The above considerations have dictated the choice of both the mirror and the wavefront sensor.

4.2 *The Deformable Mirror*

Current technology consists of supporting a thin mirror on top of piezoelectric or electrostrictive actuators. Such mirrors are well adapted to high-order correction but are poorly optimized for low-order correction which is of interest to astronomical applications. Moreover, they are technically difficult to fabricate and therefore are extremely expensive. The system proposed here is based on the use of piezoelectric bimorph wafers. Although such mirrors are not commercially available, preliminary tests made by Fred Forbes et al. 1989, at the National Optical Astronomy Observatories[1] (NOAO), have shown that they are fairly easy to fabricate and are inexpensive.

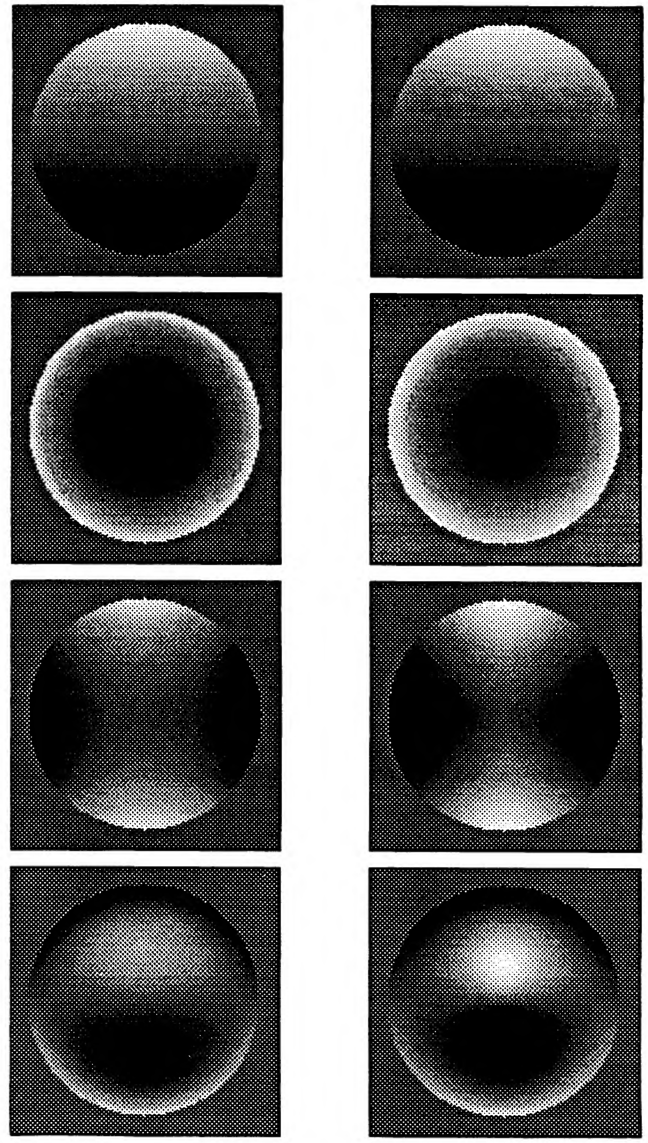

FIG. 9–Examples of Karhunen-Loeve functions (right column) together with the same-order Zernike functions (left column). From top to bottom: tilt, defocus, astigmatism, coma.

Figure 10, reprinted from their publication, shows a 37-electrode bimorph wafer made at NOAO together with the mirror response when voltage is applied to a single electrode as measured with a Zygo interferometer. A complete mirror needs additional edge controls.

A joint agreement has been established between the Office National d'Etudes et de Recherches Aerospatiales (ONERA) in France and the University of Hawaii (UH) to develop a deformable bimorph mirror with its associated wavefront sensor. UH is in charge of developing the wavefront sensor and the control electronics. ONERA has subcontracted the construction of the bimorph mirror to

[1]National Optical Astronomy Observatories are operated by the Association of Universities for Research in Astronomy, Inc., under cooperative agreement with the National Science Foundation.

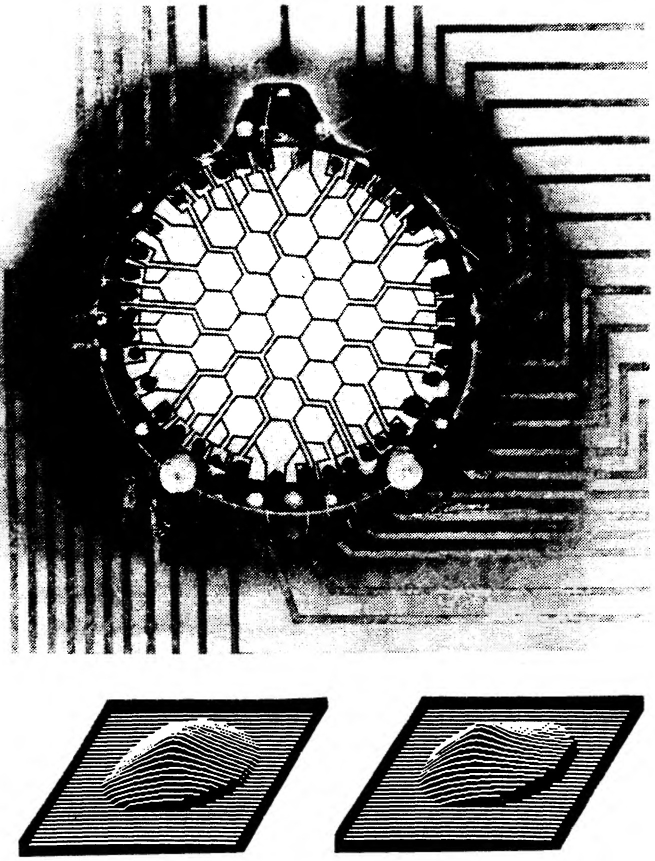

FIG. 10–Back side view of a 37-actuator bimorph mirror made by Fred Forbes at NOAO (Fred Forbes et al. 1989). It shows the control electrodes. Underneath is the mirror figure response obtained with a Zygo interferometer when exciting either the central electrode (left) or an adjacent electrode (right). Figure 13 shows the curvature sensor signal in both cases. Edge control has not been implemented yet.

LASERDOT (Laboratoires de Marcoussis, France). Preliminary studies have already been published (Jagourel, Madec & Sechaud 1990). The mirror is expected to be delivered to UH at the end of 1990.

It consists of a 5-cm-diameter bimorph wafer made of oppositely polarized piezoelectric material with 7 electrodes. The geometry of the electrodes is shown in Figure 11, reprinted from Jagourel et al. 1990. They cover only a 30-cm-diameter area which coincides with the reference beam. By applying voltage on 1 electrode one corrects the local wavefront curvature. In our current design the bimorph wafer is supported at the outer edge by 6 regularly spaced piezo stacks for edge control. These stacks will essentially control tip-tilt errors and astigmatism. The edge-control mechanism is discussed in Appendix A.1.

Compared to currently used mirrors, this technique has several advantages.

(1) By optimizing the size and shape of the electrodes, low-order aberration terms can be accurately fitted with a minimum number of applied voltages. A numerical model of the above-described mirror provided by

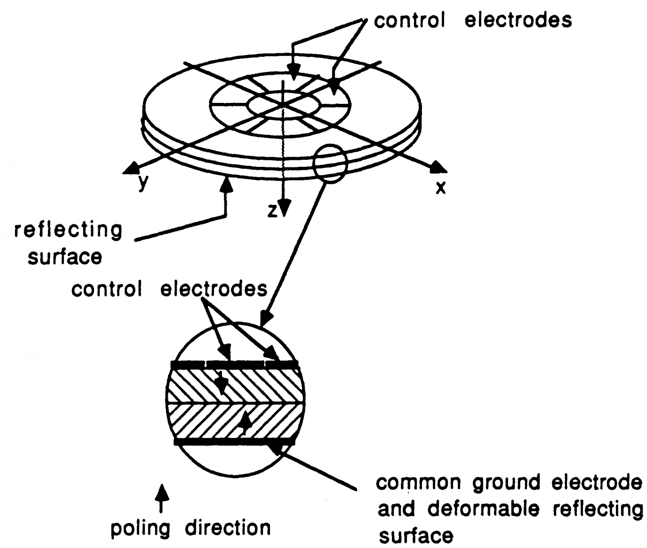

FIG. 11–Schematic of the LASERDOT deformable bimorph mirror showing the structure of the seven control electrodes (Jagourel et al. 1990). The mirror will be supported at the edge by six piezo stacks (not shown in the figure). There are a total of 13 actuators.

LASERDOT shows that, with 13 voltages, one can fit 8 Zernike terms with an accuracy better than 6% as shown in Table 4.

(2) Because the mirror is supported only at the edge, local deformations at contact points occur outside the beam. There is no print-through or "meshing" effect. A consequence is that a good mirror is fairly easy to fabricate at a moderate cost.

(3) The mirror deformation extends beyond the controlled area, providing an efficient way to further extend the isoplanatic patch size as described in Appendix B. This is essential for astronomical applications and has apparently never been considered before.

4.3 *The Wavefront Sensor*

Since a bimorph mirror corrects local wavefront curvatures, it seems natural to associate with it a sensor which measures local wavefront curvatures. This is the basis of a technique proposed by one of us a few years ago (Roddier, F. 1988). It has since been widely and successfully developed (Roddier, Roddier & Roddier 1988; Roddier, F. et al. 1990b; Roddier, C. et al. 1990). Because local wavefront curvature errors produced by the atmosphere are nearly statistically independent, curvature sensing is an efficient way to estimate atmospheric wavefront errors with a minimum number of sample points, closely matching the Karhunen-Loeve functions. Moreover, the sensitivity of a Shack-Hartmann sensor can be achieved with a very simple device requiring no calibration and a much smaller number of sensor elements, thus avoiding any precomputation (Roddier, F. et al. 1988). This is dramatically demonstrated in Table 5 which shows a comparison between curvature sensing and Hartmann sensing in AO

TABLE 4
Accuracy with which a bimorph mirror can fit Zernike modes.
(r.m.s. error as a fraction of the r.m.s. displacement)

Zernike term	2 tilt	3 tilt	4 defocus	5 astigm.	6 astigm.	7 coma	8 coma	9 tr. coma
r.m.s. error (%)	0.018	0.018	2.26	2.63	2.65	5.43	5.45	0.75

TABLE 5
Comparison between Hartmann and curvature sensors

	NOAO (Hartmann)	ESO (Hartmann)	UH (curvature)	UH (curvature)
Number of sensors	10,000	1,600	13	37
Number of measurements	37 x slopes 37 y slopes	25 x slopes 25 y slopes	7 curvatures 6 edge slopes	19 curvatures 18 edge slopes
Maximum radial degree	6	5	3	5

systems recently developed for astronomy. The third column is the system we propose to build on 4-m-class telescopes. The last column is an extension of this system to 8-m-class telescopes. The only known drawback of curvature sensing is error propagation in wavefront reconstruction which does not apply here as demonstrated in Appendix A.3.

Curvature sensing consists of comparing the illumination in two out-of-focus beam cross sections symmetrically on each side of the telescope focal plane as shown in Figure 12. Figure 13, reprinted from F. Roddier et al. 1987, shows the result obtained when two such CCD images are subtracted one from the other. In this case the 37-electrode bimorph mirror shown in Figure 10 was used and only one of the electrodes was excited. Clearly, the signal is highly localized suggesting that a simple wire-to-wire connection between the sensor and the deformable mirror will produce a good correction. This is indeed confirmed by computer simulations. By getting closer to the focal plane one increases the sensor sensitivity but decreases its spatial resolution or the number of modes one can sense with a good linear response.

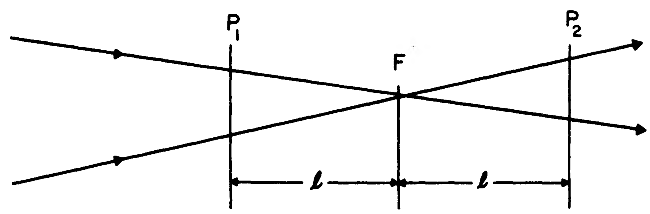

FIG. 12–Curvature sensing consists of taking the difference between the illuminations observed in two planes such as P_1 and P_2 at a distance ℓ from the telescope focal plane F.

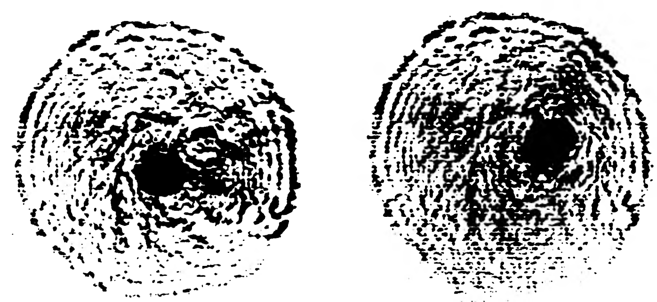

FIG. 13–Examples of curvature signals obtained by taking the difference between symmetrically defocused images recorded on a CCD camera (Roddier et al. 1987). The deformable bimorph mirror shown in Figure 10 was used to deform a plane wavefront. A single electrode was excited in each case, the central electrode (left) or an adjacent electrode (right). The corresponding mirror figure is shown in Figure 10. Note that, although the whole mirror deforms, only the area covered by the electrode produces a curvature signal.

Figure 14 is a schematic of the optical setup we propose to use. An image of the reference star is formed on a variable curvature mirror. It consists of a stretched membrane with a reflecting coating. When it is not activated, the membrane is flat and the following mirror reimages the wavefront compensator on the detector or sensor array. The membrane is activated by acoustic pressure oscillations produced by a loudspeaker. It becomes alternatively concave and convex at the acoustic oscillation frequency. When concave, it reimages an inside-focus beam cross section on the detector. When convex, it reimages the symmetric outside-focus beam cross section. This produces a modulation of the illumination on the detector. The amplitude of the modulation is proportional to the local wavefront curvature inside the pupil and to the local edge slope at the pupil edge. It therefore directly provides the signals required to drive a de-

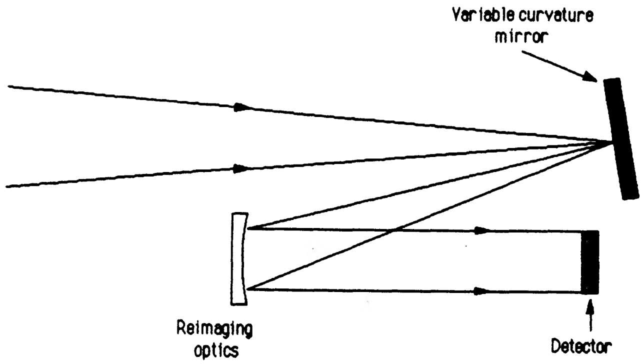

FIG. 14–Optical setup for curvature sensing. A variable curvature mirror (vibrating membrane) is located at the telescope focus. When the membrane is flat (nonactivated) the following optics reimage the telescope pupil onto the detector (sensor array). When the membrane is activated it alternatively reimages symmetrically defocused images onto the detector.

formable bimorph mirror. The frequency of the modulation is limited by the resonance frequency of the membrane but can easily reach several KHz. The sensitivity of the sensor can be modified by changing the amplitude of the vibration of the membrane, i.e., the power on the loudspeaker. In our proposed system a feedback loop is used to adjust the power on the loudspeaker to maintain the rms tip-tilt signal-error constant. Hence, the sensor will always operate in its optimum linear range and automatically adjust itself to changing seeing conditions.

4.4 *The Detector*

The detector is a key component for astronomical applications. Most systems proposed to date are based on image intensifiers which have a low quantum efficiency and a poor response in the red. A small CCD array would have a good quantum efficiency but would require a fast readout speed and would be limited by the readout noise. It is poorly suited to detect a modulated signal. We propose to use an array of 13 photon-counting avalanche photodiodes. Each diode will sense an area as shown in Figure 15. The seven inner areas provide signals proportional to the wavefront curvature, whereas the six outer areas at the beam edge provide signals proportional to the wavefront edge slope. Each measurement is, of course, an average value taken over the considered area.

Photon-counting avalanche photodiodes are now commercially available and deliver photon counts with both a good quantum efficiency and a good response in the red. With a thermoelectric cooler, the dark current can be as low as a few-hundred counts per second which is negligible over a 10-millisecond integration time. Figure 16 shows a plot of the avalanche photodiode quantum efficiency as a function of wavelength together with a rough spectral distribution of the flux from a K star. The quantum efficiency of an S-20 photocathode is also indicated for comparison. Integrated over the considered 500–900

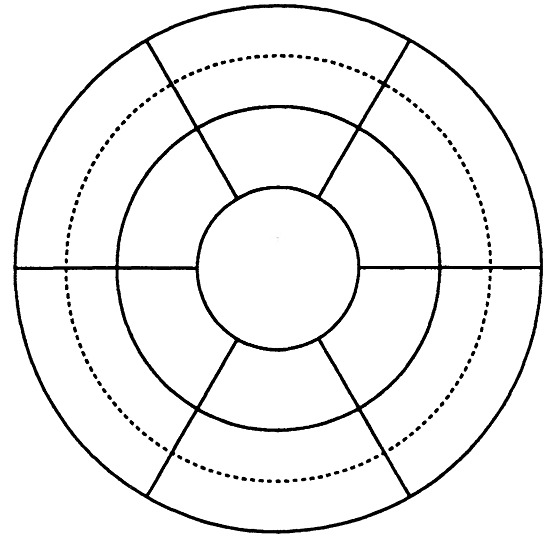

FIG. 15–Wavefront sampling geometry adopted for this proposal and used in the computer simulation. Here are shown the 13 areas over which the illumination is integrated. The pupil edge falls midway in the outer annulus (dashed line).

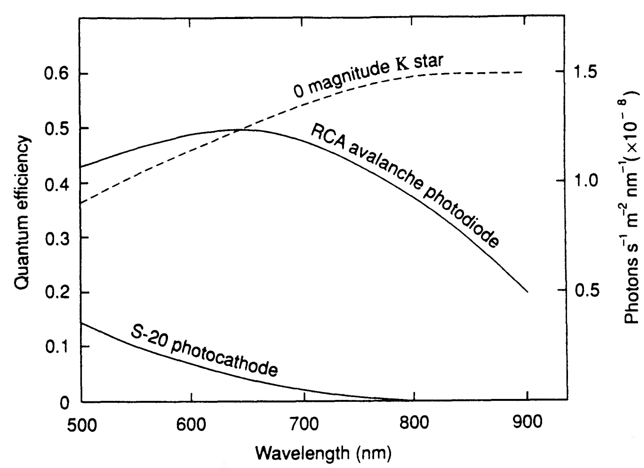

FIG. 16–Quantum efficiency of an avalanche photodiode as a function of wavelength. The quantum efficiency of an S-20 photocathode is indicated for comparison. Approximate flux distribution is given for a K star (right scale). Over the considered 0.5–0.9 μm bandwidth, photodiodes will allow us to use a reference K star 2.7 mag fainter, compared to S-20 photomultipliers.

nm bandwidth, the gain over an S-20 photocathode is 2.7 magnitudes. On a telescope such as the CFHT, each diode will receive light from a 1 m^2 area on the telescope pupil. Assuming a 70% transmission for the telescope and the atmosphere and 80% transmission for the AO system (with high reflectivity coatings), each diode will detect 5×10^3 photons/sec from an $m = 16$ star or 50 photons per 10 millisec integration time which, according to computer simulations, is the limit down to which closed-loop correction still operates reasonably well (Roddier & Roddier 1989). Occasionally, the atmosphere will allow us to operate at 40 Hz pushing the limiting magnitude up to 17.

4.5 *The Control Electronics*

For a given wavefront perturbation, the wavefront sensor delivers a set of N voltages. A control matrix **C** is used to convert these N voltages into M voltages to be applied to the wavefront compensator (deformable mirror). In the case considered here $N = M = 13$. The problem is to find the $M \times N$ control matrix that produces the optimum least-squares compensation. A general procedure is to determine the control matrix from measurements made on the system. First one determines an interaction matrix **A** by recording the N sensor responses when a single mirror actuator is activated. These measurements are repeated for the M actuators yielding an $N \times M$ interaction matrix **A**. The procedure uses a singular value decomposition of the matrix **A**

$$\mathbf{A} = \mathbf{U}\cdot\mathbf{S}\cdot\mathbf{V}^t \ , \tag{6}$$

where **S** is a diagonal matrix. The optimum control matrix **C** is the generalized inverse of **A**

$$\mathbf{C} = \mathbf{V}\cdot\mathbf{S}^{-1}\cdot\mathbf{U}^t \ . \tag{7}$$

The eigenvectors of **C** are the eigenmodes of the AO system. For an ideal system they should exactly fit the Karhunen-Loeve modes of the atmosphere. The eigenvalues are the loop gains associated with each system mode. $\mathbf{U}^t$ may be considered as a sensor matrix which describes the sensor response to each system mode. **V** is similarly a mirror matrix which determines the voltages to be applied to the mirror to compensate each system mode.

In a first phase a custom-made silicon diode array will be used with analog outputs. In this case the control algorithm will simply be hard wired using analog electronics. A general scheme is given in Figure 17. The 13 modulated signals from the sensor will be converted into about 9 modulated modal signals by simple linear combination through operational amplifiers (matrix $\mathbf{U}'$). A lock-in detection card will be used to demodulate each modal signal with a time constant appropriate to each mode (low-spatial-frequency modes are expected to have a longer evolution time). The demodulated signals will then again be linearly recombined through operational amplifiers (matrix **V**) and will provide 13 voltages to drive the deformable mirror. A 100-Hz bandwidth can easily be obtained with a modulation frequency of several KHz. We expect to produce a laboratory demonstration in early 1991 and a telescope demonstration on bright stars at the CFHT coudé focus during summer 1991.

In a second phase, avalanche photodiodes will be used and photon counts from the 13 diodes will be combined digitally during a half-cycle (matrix $\mathbf{U}^t$) while counting photons for the next cycle. The resulting modal signals will be alternatively added to and subtracted from the contents of a leaky memory producing the demodulated modal signals (lock-in detection). The outputs of the leaky

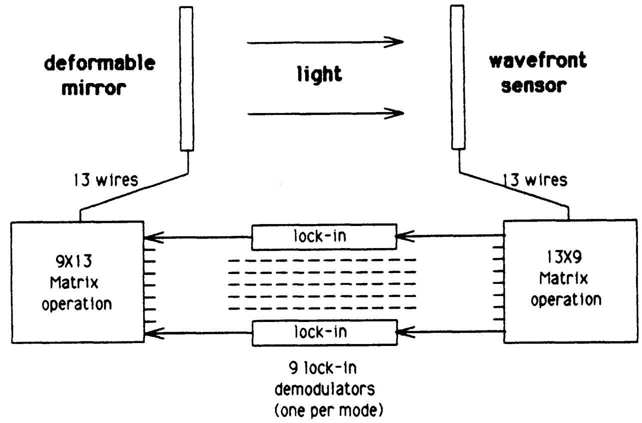

FIG. 17–Schematic of the control electronics. The 13 sensor signals are converted into 9 modal signals through the 13×9 sensor matrix $\mathbf{U}^t$ operation. Each modal signal is demodulated with a bandwidth and a gain appropriate to each mode. The 9 demodulated signals are then converted into 13 error signals through the 9×13 mirror matrix **V**. These error signals are used to update the voltages applied to the actuators which deform the mirror. In a first stage the electronics will be entirely analog. In a second stage photon counts from the diodes will be processed digitally with a microprocessor.

memory will again be combined digitally, providing data to update the voltages on the deformable mirror (matrix **V**). All this can be done at the required speed with a microprocessor and simple circuitry. A small computer will be used to control the system parameters (loop gains and time constants). One function of the computer will be to estimate the rms tip-tilt error and the wavefront lifetime and constantly optimize the system parameters.

4.6 *The Optical Scheme*

Figure 18 shows a schematic optical layout of the envisaged instrument. The light from the telescope is first focused onto a mirror M1. In a preliminary phase M1 is a flat mirror and a concave mirror M2 reimages the telescope pupil onto the deformable mirror M3. Later M1 will be replaced with a variable curvature mirror (for instance a bimorph mirror with a single electrode used to change its radius of curvature). When the electrode is activated M1 becomes convex and turbulent layers are reimaged onto the deformable mirror. By properly tuning the voltage applied to M1 one can empirically increase the isoplanatic patch size as described in Appendix A.2. The light reflected from the deformable mirror M3 goes to a high-optical-quality interchangeable dichroic beam splitter or interference filter. The near-IR light or narrow-band red light transmitted through the beam splitter is used to do astronomy. The wide-band red light reflected by the beam splitter converges to the vibrating membrane M4 which is in a plane conjugate to the telescope focal plane. The light reflected from the membrane M4 goes to a concave mirror M5. When the membrane is flat (not activated) M5 reimages the deformable mirror M3 onto the detector.

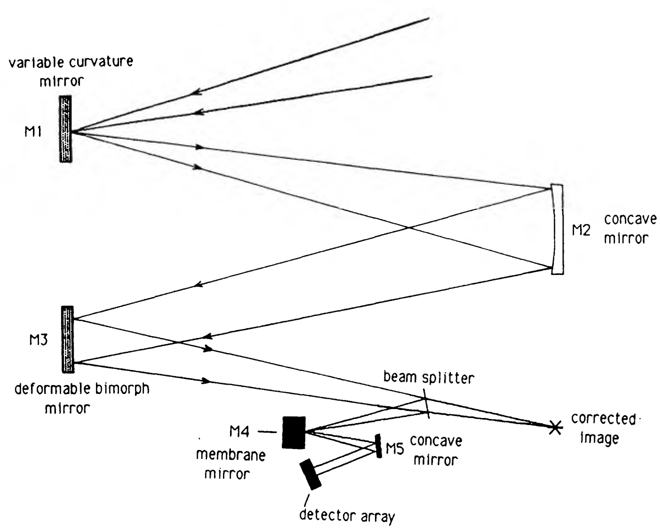

FIG. 18–Schematic of the proposed adaptive optics system for 1–2.5 µm. In the initial phase M1 is a flat mirror. M2 reimages the telescope pupil on M3. M4 and M5 form the wavefront sensor as shown in Figure 14. By changing the curvature of M1 from flat to convex one can focus the dominant turbulent layers on the deformable mirror M3 thus increasing the size of the isoplanatic patch (Section A.2).

5. Proof of Concept

5.1 *Computer-Simulation Results*

A computer model has been built of the wavefront compensation system proposed above. It consists of a random wavefront generator, a model of the wavefront sensor, and a model of the deformable mirror. The random wavefront generator, written by N. Roddier 1990, is based on a Zernike expansion of randomly weighted Karhunen-Loeve functions. It produces random wavefront surfaces the statistics of which accurately match those of atmospherically distorted wavefronts, including tip-tilt errors. A numerical model of the deformable mirror was given to us by LASERDOT. It gives the deformation of the mirror when a voltage is applied to the central electrode, to a single-side electrode, or to a single-edge support actuator. Using rotational symmetry, one can compute the mirror surface for any voltage distribution on the 13 actuators. The wavefront sensor is simulated by computing the Fresnel diffraction pattern of the distorted wavefront symmetrically on each side of the pupil plane. This is done with a fast Fourier transform (FFT) subroutine. It yields accurate estimates of the illumination including diffraction effects in the caustic zone. The sensor signals are obtained by integrating the computed illumination over designated sensor areas. We summarize here the results obtained.

A control matrix is used which computes the voltages to be applied to the simulated deformable mirror, given the sensor signals. The calculated mirror correction is subtracted from the original wavefront and the new sensor signals are calculated. Successive iterations simulate closed-loop operation. Parameters such as the amount of defocus of the out-of-focus images have been optimized. Several control matrices have been used and their performance has been compared. Figure 19 shows images with and without correction for $D/r_0 = 4$, 8, 12, and 16. These are averaged images obtained from 64 independent wavefronts. Because of the relatively small number of independent frames used, uncompensated images still show a speckle structure that would ultimately average out in a long exposure. As theory predicts, the compensated images consist of a narrow core and a halo. The core width is

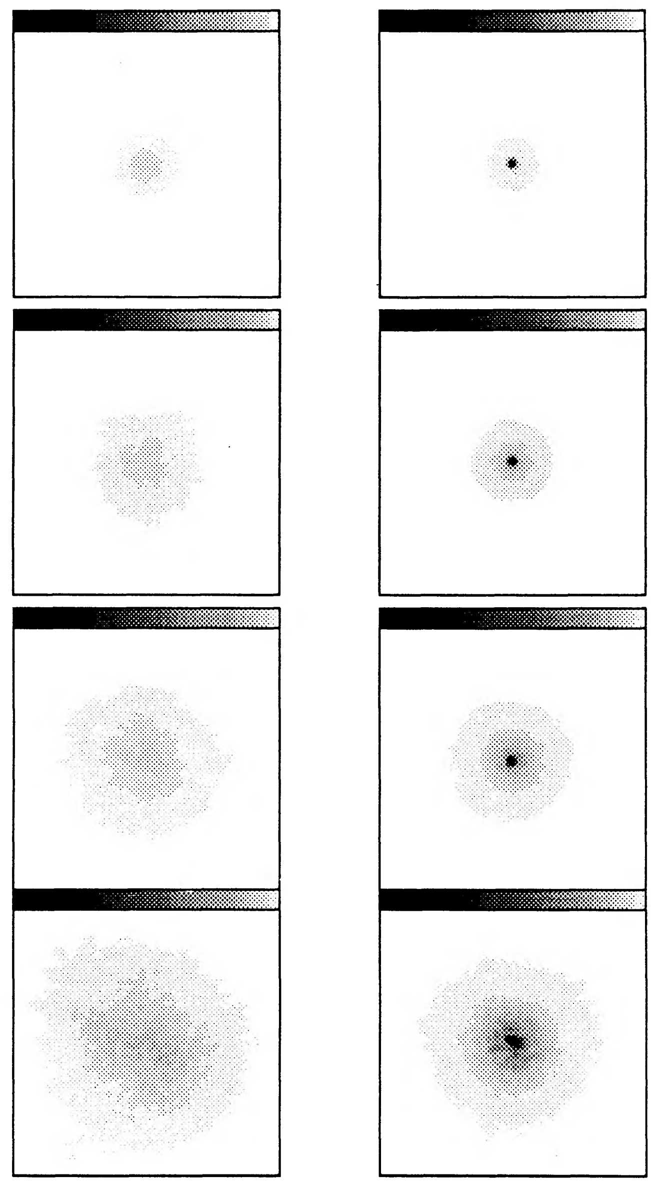

FIG. 19–Performance of the computer simulated system. Left: uncompensated images. Right: compensated images. Each image was obtained by averaging the result of 64 independent wavefronts. From top to bottom $D/r_0 = 4$, 8, 12, 16. Photometric profiles of these images are shown in Figure 4b for the $D/r_0 = 8$ case.

that of an Airy disk. When D/r_0 increases, the amount of light scattered into the halo increases. It still leaves 5% of the light in the core when D/r_0 reaches 16. Figure 4b shows a photometric profile of the compensated image when $D/r_0 = 8$. It was obtained by taking the azimuthal average of the image displayed in Figure 19. Comparison with the image profile theoretically expected under the same conditions and shown in Figure 4a demonstrates that very close to optimum performance can be obtained with our proposed configuration. Figure 20 is a plot of the normalized Strehl resolutions observed in the simulation together with the theoretical curves shown in Figure 1. Clearly, the performance of the simulated system is close to the theoretical limit. For comparison, we have also plotted the results of the European "COME-ON" experimental system obtained in France at the Haute Provence Observatory (Rousset et al. 1990a). Different D/r_0 values correspond to different wavelengths. The drop of the Strehl resolution at $D/r_0 \approx 5$ can be explained by the insufficient bandwidth of the system.

5.2 *Experimental Results*

A curvature sensor has been built with a vibrating membrane (Fig. 21) and closed-loop operation has been demonstrated in the lab. Since we do not yet have a deformable mirror, the demonstration was limited to tip-tilt correction. The setup is shown in Figure 22. Two tip-tilt mirrors are used, one to produce image motion and the other to correct it. An image of a point source is formed on the vibrating membrane. The light reflected by the membrane goes through a lens which reimages the entrance pupil onto the detector as also shown in Figure 14. For this experiment the detector is a commercial quadrant of four photodiodes. When the star image moves away from the center of the membrane, the pupil image starts to oscillate along the same direction on the quadrant detector producing modulated output signals.

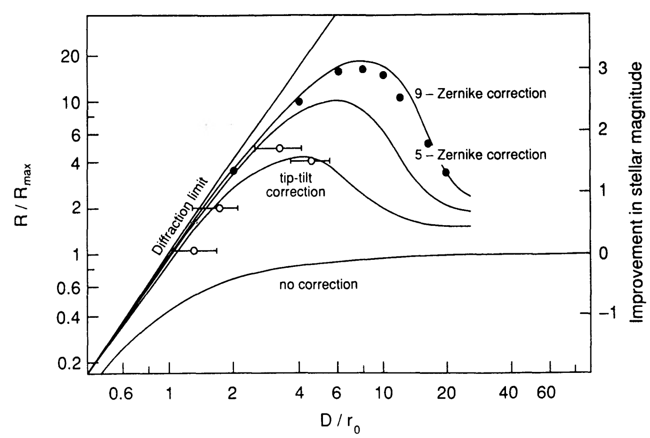

FIG. 20–A comparison between the performance of our simulated system (black dots) and that expected from theory (see Fig. 2). Open circles show the performance of the European AO system COME-ON which has a 19-actuator mirror (the horizontal bar is the uncertainty on the seeing estimate).

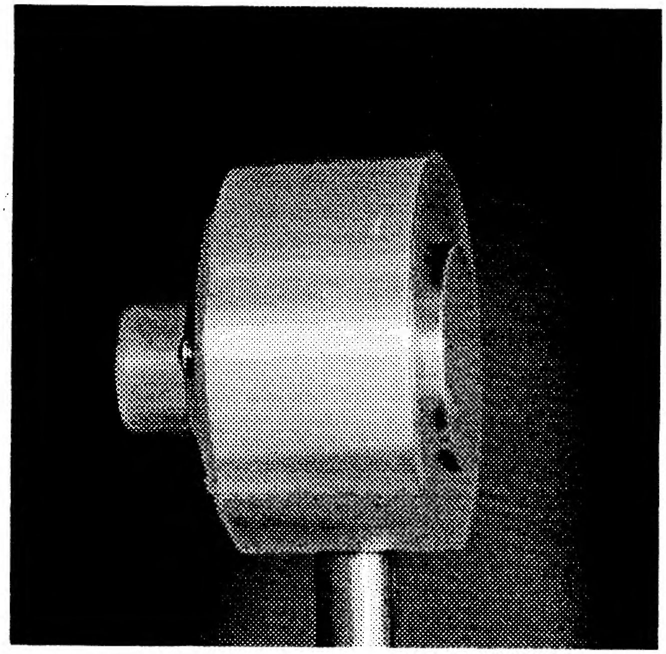

FIG. 21–Photograph of the membrane mirror used to modulate the curvature sensor signals. Acoustic pressure from the loudspeaker behind forces the membrane to vibrate.

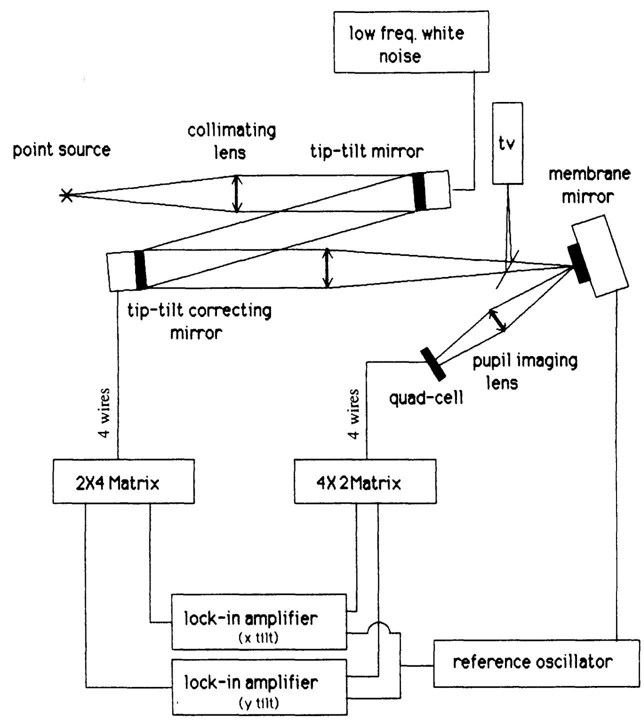

FIG. 22–Experimental setup used to test curvature sensing in closed-loop operation. The test successfully performed in February 1990 was limited to tip-tilt corrections. The 4 × 2 sensor matrix and the 2 × 4 mirror matrix operation are performed by standard commercial devices. Note that the control electronics shown in Figure 17 is a straightforwad extension of the same scheme.

The amplitude of the modulation is proportional to the offset distance. The phase of the modulation changes by

180° when the star image moves in the opposite direction. The signals from the quadrant detectors are converted into modulated x and y tilt error signals using commercial analog electronics usually sold with quadrant detectors. Lock-in amplifiers are used to demodulate the signals, with the loudspeaker drive voltage as a reference. The demodulated x and y tilt error signals are used to drive a commercial tip-tilt corrector which consists of a mirror mounted on four piezo stacks. The mirror comes with analog electronics which convert the two tilt error signals into four voltages, one for each stack. Note that the electronics exactly follow the scheme described in Section 4.5 and illustrated in Figure 17, but for the size of the matrices. Here the sensor matrix is 4×2 and the mirror matrix is 2×4. In this case both matrix operations are performed by standard commercial analog electronics. Since we control only two modes, there are only two lock-in demodulators. Our proposed wavefront compensation system is a straightforward extension of this very simple scheme.

It is worth comparing the above-described tip-tilt compensation scheme to current image stabilizing devices. In current systems such as the CFHT HR Camera, the reference source is reimaged onto the quadrant detector. In the above-described approach the telescope pupil is reimaged onto the quadrant detector. This new approach has several advantages:

(1) Because the pupil image oscillates on the detector and the output signals are inverted every half-cycle (lock-in demodulation), the error signal becomes totally independent of the gains of the four quadrants. The system is therefore immune to gain drifts which plague current systems.

(2) The field of acquisition is limited by the membrane size, not by the detector size. Hence, one can have a wide field of acquisition with a small quadrant detector, thus limiting detector noise or dark current.

(3) Quadrant detectors have a highly nonlinear response which severely limits the dynamic range of current systems. By changing the amplitude of the membrane vibration, one can always match the error signal to the linear part of the detector response. This can even be done automatically in a servoloop, thus producing a tilt sensor with considerable dynamic range.

(4) On extended objects each object point contributes linearly to the modulation. As a consequence, the sensor signal gives the displacement of the exact center of "gravity" of the object. For instance, current sensors would fail to track a double star with two components of equal magnitude, one on each opposite quadrant. Our sensor accurately tracks the center of "gravity" of the two components.

(5) By using more than four detectors one can easily detect higher-order Zernike modes as we intend to do.

6. Conclusion

It is currently believed that, on a 4-m class telescope, several tens of correcting elements are required to achieve compensation in the infrared and several hundreds in the visible. We have shown that low-order correction can lead to substantial improvement in image quality. For example, a simple tip-tilt 2-Zernike correction can reduce the image size by one-half at 1.2 μm; a 9-Zernike correction can achieve nearly diffraction-limited images at wavelengths equal to or longer than 0.7 μm (Fig. 2b). By keeping the number of compensated Zernike terms small, one makes the reference star required as faint as $m = 17$ in the visible. In addition, one makes the isoplanatic patch size large enough to take full advantage of the correction over most of the sky (Table 2).

Currently proposed AO systems are not optimized for low-order correction. A novel, more optimized approach has been described, which allows high-speed compensation to be achieved with high-sensitivity detectors. Computer-simulation results show that the proposed system can achieve the desired performance. Closed-loop operation has been demonstrated in the laboratory on tip-tilt corrections.

The authors want to thank Don Hall and Len Cowie for supporting this work with UH funds. They also want to thank Marc Séchaud, Pierre-Yves Madec, and Gérard Rousset for getting support from ONERA and J. P. Gaffard and Pascal Jagourel for their willingness to fabricate the mirror and for the computer model they provided. This work is also now partly supported by a grant from the Strategic Defense Initiative Organization, Office of Innovative Science and Technology, and managed by the Harry Diamond Laboratories. The authors also wish to acknowledge the input of many colleague astronomers, particularly John Kormendy, René Racine, Alan Tokunaga, and Hans Zinnecker.

APPENDIX

A.1 *Mirror Edge Control*

Edge control is a key issue in bimorph mirror technology. Once local curvatures (Laplacians) are compensated on the incoming wavefront, one is left with zero-Laplacian modes which also have to be compensated. These modes have the following form

$$Z_n(r, \theta) = r^n \cos n\,\theta \ . \tag{8}$$

At the pupil edge ($r = R$), the radial slope is proportional to the wavefront error

$$\frac{\partial Z_n}{\partial r} = \frac{n}{R} Z_n (R, \theta) \ . \tag{9}$$

It is therefore possible to use wavefront-edge, radial-slope measurements to control the position of the mirror edge. However, the gain of the servoloop will be proportional to the degree n of the mode. To avoid instabilities, one can make a Fourier decomposition of the measured edge slopes and adjust the gain for each mode. Hence, a modal control algorithm will work, as confirmed by computer simulations.

A.2 *Isoplanicity Tuning*

High-altitude turbulent layers severely reduce the isoplanatic patch size by producing object and reference wavefront errors which are identical but at a different location on the telescope pupil. If there were a single turbulent layer, one could considerably increase the isoplanatic patch size by reimaging the layer onto the deformable mirror, thus making the wavefront errors in the two beams coincide (see, for instance, Roddier, F. 1981). As a result the object beam is shifted sideways from the reference beam (as it is at the altitude of the layer) and part of it falls outside the controlled area on the deformable mirror. If not vignetting, currently used mirrors produce no deformation outside the controlled part. In our proposed system, a bimorph mirror is used which is larger than the controlled area and extrapolates the measured wavefront with a zero curvature surface and no discontinuity of the first derivatives. It also interpolates the wavefront inside the pupil central obstruction. As a consequence, it will still provide a reasonable correction outside the reference beam area. Clearly, wavefront extrapolation is a key to increasing the isoplanatic patch size.

In practice many turbulent layers contribute to image degradation at different altitudes. However, there is necessarily an optimum altitude which, focused onto the deformable mirror, will produce the largest isoplanatic patch. The optical scheme described in Section 4.6 and illustrated in Figure 18 will allow us to control continuously the amount of pupil defocus and to maximize the optimum isoplanatic patch as seeing conditions vary. The technique will be tried after the initial tests of the AO system. Theoretical considerations show that one should be able to increase the isoplanatic patch size by an amount at least equal to the one discussed in F. Roddier, Gilli & Vernin 1982, i.e., easily up to a factor two depending on seeing conditions. By the same token one will also decrease the amount of image degradation due to amplitude fluctuations (scintillation).

A.3 *Error Propagation*

The only known drawback of curvature sensing is that the error in wavefront reconstruction increases with the number of sample points faster than that of a Hartmann sensor. This can be explained as follows. In order to reconstruct a wavefront over P points a Hartmann sensor requires $2P$ measurements, P_x slopes and P_y slopes. A curvature sensor requires $P + Q$ measurements, P curvatures, and Q edge slopes. P increases as the pupil area, but Q increases only as the pupil linear size. Hence, for large sensor arrays, Hartmann sensors provide more wavefront information and are, therefore, less subject to error propagation. However, for small arrays such as those considered for astronomical applications, Q can be equal to or even larger than P, in which case curvature sensing is to be preferred. To illustrate this point Figure 23 shows the values of P and Q for arrays of increasing size with a regular hexagonal sampling over a full circular pupil. It shows that, up to 37 measurements, curvature sensing is appropriate. In our proposed sampling geometry, shown in Figure 15, we have only 7 curvature measurements. We have limited the number of edge-slope measurements to 6 which still gives us near-Hartmann-equivalent performance. We can sense up to 11 Zernike terms. On a large 8-m-class telescope, one could use a larger array with 19 curvature measurements and 18 slope measurements, as shown in Figure 23 (see also last column in Table 5) and still get Hartmann-equivalent performance.

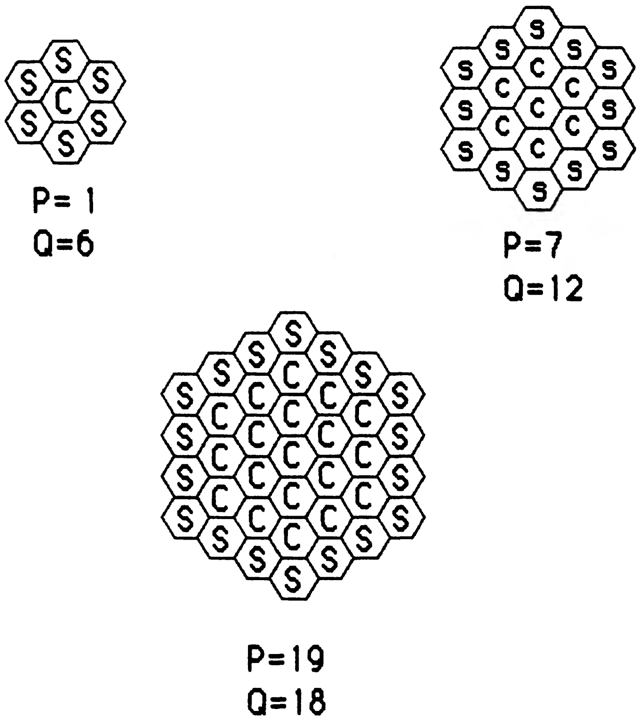

FIG. 23–Examples of possible wavefront sampling for a curvature sensor. *C*'s are curvature (Laplacian) measurements. *S*'s are edge slope measurements. *P* is the number of curvature measurements and *Q* is the number of slope measurements. Curvature sensing is superior or equivalent to Hartmann sensing as long as $Q \geq P$.

REFERENCES

Babcock, H. W. 1953, PASP, 65, 229
———. 1990, Science, 249, 253
Brown, D. S., Doel, A. P., Dunlop, C. N., Major, J. V., Myers, R. M., Purvis, A., & Thompson, M. G. 1988, in ESO Conf. 30, Very Large Telescopes and Their Instrumentation, ed. M. H. Ulrich (Garching, ESO), p. 761
Buffington, A., Crawford, F. S., Muller, R. A., & Orth, C. D. 1977, J. Opt. Soc. Am., 67, 304
Chassat, F. 1989, J. Opt. (Paris), 20, 13
Christian, C., & Racine, R. 1985, PASP, 97, 1215
Forbes, F., Roddier, F., Poczulp, G., Pinches, C., Sweeney, G., & Dueck, R. 1989, J. Phys. E: Sci. Instrum., 22, 402
Fried, D. L. 1966, J. Opt. Soc. Am., 56, 1372
Hardy, J. W. 1981, in ESO Conf., The Scientific Importance of High Angular Resolution at Infrared and Optical Wavelengths, ed. M. H. Ulrich & K. Kjär (Garching, ESO), p. 25
———. 1982, SPIE Conf., 332, 252
Hufnagel, R. E. 1974, OSA Topical Meeting on Optical Propagation through Turbulence, Boulder, Colorado, Technical Digest, Wa1
Jagourel, P., Madec, P. Y., & Séchaud, M. 1990, SPIE Conf., 1237, 394
Kern, P., Lena, P., Rousset, G., Fontanella, J. C., Merkle, F., & Gaffard, J. P. 1988, in ESO Conf. 30, Very Large Telescopes and Their Instrumentation, ed. M. H. Ulrich (Garching, ESO), Vol. II, p. 657
Kern, P., Lena, P. J., Rousset, G., Merkle, F., & Rigaut, F. 1990, SPIE Conf., 1237, 345
Lena, P. 1988, Observational Astrophysics (Springer Verlag)
Maaswinkel, F., Bortoletto, F., Buonanno, R., Buzzoni, B., D'Odorico, S., Gilli, B., Huster, G., & Nees, W. 1988, in ESO Conf. 30, Very Large Telescopes and Their Instrumentation, ed. M. H. Ulrich (Garching, ESO), p. 751
Major, V., Doel, A. P., Dunlop, C. N., Myers, R. M., Purvis, A., & Thompson, M. G. 1990, SPIE Conf., 1236, 179
McClure, R. D., et al. 1989, PASP, 646, 1156
Racine, R., & McClure, R. D. 1989, PASP, 101, 731
Roddier, C., Roddier, F., Stockton, A., & Pickles, A. 1990, SPIE Conf., 1236, 756
Roddier, F. 1981, Prog. Opt., 19, 352
———. 1988, Appl. Opt., 27, 1223
Roddier, F., et al. 1990a, SPIE Conf., 1236, 485
Roddier, F., Forbes, F., Shaklan, S., & Pinches, C. 1987, in Adaptive Optics in Solar Observations, ed. O. Engvold (Federal Republic of Germany, Kiepenheur Inst.), p. 176
Roddier, F., Gilli, J. M., & Vernin, J. 1982, J. Opt. (Paris), 13, 63
Roddier, F., Graves, J. E., & Limburg, E. 1990b, SPIE Conf., 1236, 474
Roddier, F., Roddier, C., & Roddier, N. 1988, SPIE Conf., 976, 203
Roddier, N. 1990, SPIE Conf., 1237, 668
Roddier, N., & Roddier, F. 1989, SPIE Conf., 1114, 92
Rousset, G., et al. 1990a, SPIE Conf., 1237, 336
———. 1990b, A&A, 230, L29
Smithson, R. C., & Peri, M. L. 1989, J. Opt. Soc. Am. A, 6, 92
Tokunaga, A. T. 1989, Ap. Space Sci., 160, 333
Valley, G. C., & Wandzura, S. M. 1979, J. Opt. Soc. Am., 69, 712
Wang, J. Y., & Markey, J. K. 1978, J. Opt. Soc. Am., 68, 78